

# The Gamma–Ray Burst catalog obtained with the Gamma Ray Burst Monitor aboard *BeppoSAX*

F. Frontera<sup>1,2</sup>, C. Guidorzi<sup>3</sup>, E. Montanari<sup>1,4</sup>, F. Rossi<sup>1</sup>, E. Costa<sup>5</sup>, M. Feroci<sup>5</sup>, F. Calura<sup>6</sup>, M. Rapisarda<sup>7</sup>, L. Amati<sup>2</sup>, D. Carturan<sup>1</sup>, M. R. Cinti<sup>5</sup>, D. Dal Fiume<sup>2</sup>, L. Nicastro<sup>2</sup>, M. Orlandini<sup>2</sup>

## ABSTRACT

We report on the catalog of Gamma–Ray Bursts (GRBs) detected with the Gamma Ray Burst Monitor aboard the *BeppoSAX* satellite. It includes 1082 GRBs with 40–700 keV fluences in the range from  $1.3 \times 10^{-7}$  to  $4.5 \times 10^{-4}$  erg cm $^{-2}$ , and 40–700 keV peak fluxes from  $3.7 \times 10^{-8}$  to  $7.0 \times 10^{-5}$  erg cm $^{-2}$  s $^{-1}$ . We report in the catalog some relevant parameters of each GRB and discuss the derived statistical properties.

*Subject headings:* gamma rays: bursts — gamma rays: observations — X-rays: general

## 1. Introduction

In the last ten years a big step forward has been accomplished in the Gamma Ray Burst (GRB) astronomy. A key role in this advancement has been played by the *BeppoSAX* satellite (Boella et al. 1997). Its capability of promptly and accurately localizing GRBs and the possibility of following them up with highly sensitive X-ray telescopes on-board allowed the

---

<sup>1</sup>Università di Ferrara, Dipartimento di Fisica, Via Saragat 1, 44100 Ferrara, Italy; email: frontera@fe.infn.it

<sup>2</sup>INAF/Istituto di Astrofisica Spaziale e Fisica Cosmica, Bologna, Via Gobetti 101, 40129 Bologna, Italy

<sup>3</sup>INAF, Osservatorio Astronomico di Brera, Via Bianchi 46, 23807 Merate, Italy

<sup>4</sup>Istituto IS Calvi, Finale Emilia (MO), Italy

<sup>5</sup>INAF/Istituto di Astrofisica Spaziale e Fisica Cosmica, Roma, Via del Fosso del Cavaliere 100, 00133 Roma, Italy

<sup>6</sup>Dipartimento di Astronomia, Università di Trieste, Via G. B. Tiepolo 11, 34131 Trieste, Italy

<sup>7</sup>ENEA Divisione Fusione, Centro Ricerche di Frascati, CP 65, 00044 Frascati, Rome, Italy

discovery of the X-ray afterglow emission and, with ground telescopes, of the optical/radio afterglow from GRB sources (Costa et al. 1997; van Paradijs et al. 1997; Metzger et al. 1997; Frail et al. 1997). In this way the distance scale of long ( $>1$  s) GRBs could be eventually established and important information on the GRB sources, their emission mechanisms and their environments could be derived.

The two *BeppoSAX* instruments that allowed the prompt and accurate GRB localization were the Gamma Ray Burst Monitor (GRBM) and the two Wide Field Cameras (WFC), the first with the role of recognizing the occurrence of a GRB and second with the role of localizing it in the case the event direction occurred in their field of view ( $40^\circ \times 40^\circ$  full width at zero response) and was above the instrument sensitivity in their operative energy range (2–28 keV) (Jager et al. 1997). Only a handful of GRBs (50, see Frontera 2004,) was detected with both instruments, while the GRBM alone detected 1082 GRBs, a number similar to that of GRBs included in the third BATSE (3B) burst catalog (Meegan et al. 1996). In this paper we present the catalog of these GRBs with their main observational and statistical properties.

## 2. Instrumentation

The *BeppoSAX* GRBM was part of the high energy experiment PDS (Phoswich Detection System, Frontera et al. (1997)), being its anti-coincidence (AC) shield. It was composed of four independent detection units, made of slabs of CsI(Na)scintillators, forming the four sides of a square box (see Fig. 1). Each slab was 1 cm thick and had a geometric area of 1136 cm<sup>2</sup>, with an open field of view. The light scintillation produced in each unit was viewed by two photo-multipliers. A calibration source, made of Am<sup>241</sup>, embedded in a NaI(Tl) crystal, allowed to monitor the instrument gain. The gain could be varied by changing the HV supply of each GRBM unit.

The electronics associated to the GRBM was a simple spectroscopic chain in which the signals from each of the four detection units between two analog thresholds, after being multiplexed, were analog-to-digital converted by an ADC. By telecommand the low level threshold (LLT) could be varied in the nominal energy range from 20 to 90 keV (16 steps), while the upper level threshold (ULT) could be varied between 200 and 700 keV (8 steps). The signals detected by each unit between LLT and ULT (good events) and above the AC threshold (ACT) were continuously counted with a 1 s integration time and stored in the on-board memory. The ACT could be selected between 100 and 300 keV (8 steps). The GRBM electronic unit included an on-board GRB trigger (see § 2.1). If the on-board trigger condition was satisfied for at least two detection units, then the following high time resolution

profiles for each of the GRBM units were stored on board and then transmitted to ground:

- 7.8125 ms time profiles from the trigger time back to 8 s before;
- 0.48828125 ms time profiles from the trigger time to 10 s later;
- 7.8125 ms time profiles from 10 s after the trigger time for 88 s.

In addition to these data, for each detection unit, the following data were continuously transmitted:

- 1 s count rates between LLT and ULT;
- 1 s count rates above ACT (in phase with the previous ones);
- 240 channel spectra of the signals between LLT and ULT, integrated over 128 s (synchronous integration, in phase with the 1 s count rates).

Further details about the GRBM instrument can be found elsewhere (Amati et al. 1997; Feroci et al. 1997; Costa et al. 1998).

### 2.1. On-board and on-ground GRB trigger logic

The GRBM electronic unit included an on-board GRB trigger logic (OBTL) that worked in the following way. For each GRBM unit and for the events with amplitudes between LLT and ULT with a binning time of 7.8125 ms, a moving average on a Long Integration Time (LIT) was continuously computed. The LIT was adjustable from the ground between 8 and 128 s. The counts integrated over a Short Integration Time (SIT), also adjustable between 7.8125 ms and 4 s, were thus compared with the LIT moving average normalized to the same integration time. If the count difference exceeded  $n$  ( $n = 4, 8$ , or  $16$ ) times the Poissonian standard deviation  $\sigma$  of the mean count rate, then the trigger condition for that unit was satisfied. As seen above, the GRB trigger was activated when the trigger condition was satisfied for at least 2 detection units.

As discussed below, the OBTL was not suitable to distinguish between true GRBs and many other spurious events, like the crossing of high energy charged particles, atmospheric phenomena, etc. In addition, it was not able to detect weak events, that were recognized as GRBs only by visual inspection of the 1 s ratemeters; also it was not operative during the

transmission of the high time resolution data to the on-board tape recorder. In the latter case, only a flag about the occurrence of a burst-like event was transmitted.

In order to reject spurious events and/or to increase the GRB detection rate, we implemented a ground software (Guidorzi et al. 2001) which was capable to perform a prompt analysis of the GRBM data transmitted each orbit when the satellite was visible by the Malindi (Kenya) ground station. The SW trigger conditions (SWTC) were the following. As in the case of the OBTL, for each GRBM detection unit the count level in the 40–700 keV and  $> 100$  keV nominal energy bands was continuously monitored by performing a moving average integrated over 100 s time interval. A SW trigger was generated each time the counting rate either in both energy bands for at least two detection units, or in both energy bands for only one unit whose axis was directed toward the sky, or only in the 40–700 keV band for at least three detection units, was  $n\sigma$  higher than the last estimate of the moving average, with  $n = 6$  in the 40–700 keV band, and  $n = 3$  in the  $> 100$  keV channel. The condition for the  $> 100$  keV channel was of key importance for recognizing a true GRB event and to reject spikes due to high energy particles, whose energy release in the GRBM detectors showed a soft spectrum.

### 3. GRBM response function

The determination of the GRBM response function, both in direction and energy, was performed with Monte Carlo techniques and tested with ground calibrations performed before the *BeppoSAX* launch and with various observations of the the Crab Nebula. It was also cross-calibrated with the BATSE experiment (Fishman et al. 1994).

The GRBM response function derived via Monte Carlo code (Rapisarda et al. 1997) made use of the Monte Carlo N-Particle Transport Code (MCNP), version 4.2, released by the Los Alamos National Laboratory (LANL) (for the current MCNP version see Brown (2002)). The code allows to transport photons, neutrons and electrons from 1 keV to 100 MeV through matter. Every kind of three-dimensional geometry could be described by defining separate cells with composition and density chosen by the user. Photon interactions were treated very accurately and the entire satellite was modeled with a high degree of detail.

The model was tested using the GRBM ground calibrations performed before the flight when the instrument was integrated in the spacecraft (Amati et al. 1997). Preliminary results of these tests were reported (Calura et al. 2000).

The response function, obtained with the Monte Carlo code, was determined as a function of the energy and direction of the incident photons. Using as reference frame the satellite

local frame with equatorial plane perpendicular to the axis of the Narrow Field Instruments ( $z$  axis), and using as polar axis the  $z$  axis, a grid of 576 directions was determined: 36 azimuthal angles  $\phi_k$  in the range 0 to 360 degrees, in which the zero value corresponds to the azimuth of the axis of the detection unit #2, and 16 polar angles  $\theta_j$  in the range  $-70 < \theta < +80$  degrees. Ten different intervals of the photon energy  $E_n$  ( $n = 1, 11$ ) in the 30 to 1000 keV were also simulated with logarithmic steps. For each grid point we determined the expected number of counts  $N_i(E_n, \theta_j, \phi_k)$  detected in the 40–700 keV and  $> 100$  keV channels by each of the 4 detection units ( $i = 1, 2, 3, 4$  for detections by the units #1, #2, #3, #4 in the 40–700 keV channel, and  $i = 5, 6, 7, 8$  for detections by the same units in the  $> 100$  keV channel), for an input photon of energy  $E_n$  incident from the direction  $(\theta_j, \phi_k)$ .

A further refinement of the grid was obtained by interpolating with cubic splines  $N_i(E_n, \theta_j, \phi_k)$  in both energy and direction. The grid energy was refined up to 1 keV steps and the direction  $(\theta_j, \phi_k)$  was refined up to  $(1^\circ, 1^\circ)$  steps. Assuming a photon spectrum  $I(E) = Kf(E, \alpha)$ , where  $\alpha$  are the model parameters, for a photon beam coming from the direction  $(\theta_j, \phi_k)$  we expect to detect from each detection unit the following count rate in the above energy channels by each detection unit:

$$C_i(\theta_j, \phi_k, \alpha, K) = \sum_n \Delta E_n K f(E_n, \alpha) N_i(E_n, \theta_j, \phi_k) \quad (1)$$

The best estimate of the GRB arrival direction  $(\theta, \phi)$  and of the parameters  $\alpha$  of the assumed photon spectrum is determined by minimizing the following  $\chi^2$  statistics (for a power-law photon spectrum, see Calura et al. (2000)):

$$\chi^2(\theta_j, \phi_k, K, \alpha) = \sum_{i=1}^8 \frac{1}{\sigma_i^2} \left( n_i - \frac{n C_i(\theta_j, \phi_k, K, \alpha)}{C(\theta_j, \phi_k)} \right)^2 \quad (2)$$

where  $n_i$  is the measured counting rate measured by the unit  $i$  as above defined,  $\sigma_i^2$  is the variance of  $n_i$ ,  $n = \sum_{i=1}^8 n_i$ , and  $C(\theta_j, \phi_k) = \sum_{i=1}^8 C_i(\theta_j, \phi_k, K, \alpha)$ .

Actually, given that we had only two energy channels, we were constrained to use as input model  $f(E, \alpha)$  a simple power-law ( $E^{-\Gamma}$ ). The best estimate of the parameters  $(\theta, \phi, K, \Gamma)$  was that which minimized the  $\chi^2$  in the eq. 2. In the case that more solutions were found for  $(\theta, \phi)$ , no localization or spectrum is included in the catalog.

## 4. In-flight performance

### 4.1. In-flight settings

The values of the GRBM thresholds and trigger parameters were set and varied during the *BeppoSAX* mission (inclination orbit of  $3.9^\circ$ , initial altitude of 600 km) according to Table 1. The initial low energy threshold (32.5 keV) was risen to 42.5 keV in October 1996 in order to suppress the spiking noise and to decrease the background level, without a significant change of the source signal given the small transparency of the GRBM at low energies due to payload materials in its Field of View (FOV) (see Fig. 1). With the new low-energy threshold and the new setting of the GRB trigger parameters (see Table 1), about 12 triggers per day occurred ( $\sim 0.8$  triggers per orbit), most of which were false. The false triggers were due to correlated events in two contiguous detection units. These events were mainly due to charged particles which crossed two detection units. Indeed we found that false triggers were composed of fast events (less than 10 ms duration) with slightly different time profiles in two contiguous detection units.

The decrease of the LIT from 128 s to 32 s in November 1996 (see Table 1) was motivated by the need of a correct evaluation of the background level when the satellite was approaching to the South Atlantic geomagnetic Anomaly (SAA). Indeed we found that 10 minutes before SAA the background significantly increased below 100 keV, sometimes dramatically. One of these rapid variations occurred during the orbit in which we detected the famous GRB event of 28 February 1997 (Costa et al. 1997). We called these rapid background variations pre-SAA effects (Feroci et al. 1997).

The last change of the GRB trigger parameters, in particular of the SIT, was performed in 2002, a few months before the end of the *BeppoSAX* operative life, in order to make the GRB trigger more sensitive to short GRBs.

### 4.2. Background estimate and its subtraction

The GRBM was nominally performing since the satellite launch (Feroci et al. 1997). The background level along the orbit, outside the region near the SAA, remained very stable, with an average variation  $\leq 10\%$ . Because of the background stability, the background subtraction for the GRB data analysis was in general not critical, except for very weak events occurring close to the SAA and, for spectral evolution analysis, during the initial onset and tails of weak events. For the ratemeters data, the background during the event was estimated by interpolating the data taken  $\sim 250$  s before and after the event with a polynomial, the order

of which was chosen on the basis of the local background variation level. In the case of the 240-channel spectra, polynomials were used to interpolate the background trend in different energy ranges using 3 (or more) packets (each one covering 128 s) before and after the packet (0 or more packets) containing the event spectrum.

## 5. In flight test of the GRBM response function

After background subtraction, GRBM data were analyzed using the response matrix described above, which had also been converted to FITS format to be used with standard spectral analysis software packages like XSPEC.

The goodness of the response matrix was verified in flight with the Crab Nebula observed via source occultation by the Earth (Guidorzi et al. 1998) and with cross-checks with BATSE results obtained for a GRB selected sample by Kaneko et al. (2006).

The Crab flux and spectrum were derived using both the 2-channel ratemeters and the 240-channel spectra. We found the spectral parameters consistent with the corresponding values found with other experiments in hard X-/soft gamma-rays, i.e. a photon index of about 2.2 and a 100 keV flux density of about  $60 \times 10^{-5}$  photons  $\text{cm}^{-2} \text{ s}^{-1} \text{ keV}^{-1}$ , with reduced  $\chi^2$  values of about 1.3 for about 13 d.o.f. By fixing the photon index at the commonly adopted X-rays value of 2.1, we obtain a normalization at 1 keV of  $9.64 \pm 0.49$  photons  $\text{cm}^{-2} \text{ s}^{-1} \text{ keV}^{-1}$ , which is fully consistent with the classical value of 9.7 (Toor & Seward 1974).

Cross-checks with BATSE results were performed with a sample of 46 strong GRBs detected by both experiments and arriving from various directions. The results show that the ratio of the 40–700 keV fluences derived from the GRBM response function with those derived using spectral law, parameters and time integration given by Kaneko et al. (2006), is distributed according a Gaussian centered at about 0.8 with a standard deviation of 0.3. The deviation of the ratio mean value from 1 and the distribution spread are a likely consequence of the uncertainties in the response functions and GRB directions, and of the differences in integration time and spectral models adopted by us and by the above authors.

The uncertainty in the knowledge of the GRBM response function is on average of the order of 10%. This uncertainty is mainly due to the error in the knowledge of the flux of the calibration sources and to the errors in the calibrations data. This uncertainty was added in quadrature to that on the GRB count spectra before performing the fits.

## 6. Sky exposure

The GRBM sky exposure, that is the fraction of time above the horizon in which a given sky direction was exposed to the GRBM, is shown in Figure 2, in celestial coordinates. As can be seen, the celestial poles were never blocked by the Earth and thus they were continuously visible by the GRBM, while the other sky directions, due to the *BeppoSAX* orbit, were monitored for a shorter time. The dependence of the sky exposure on the right ascension was very small, while that on the declination is shown in Fig. 3, after averaging the sky exposure over the right ascension.

## 7. The Catalog

In Table 2 we show the GRBM catalog of GRBs. A preliminary version of the catalog can be found elsewhere (Guidorzi 2002), where the peak fluxes and fluences were given in counts (no correction for efficiency). The catalog includes 1082 events. The parameters associated to each event include the best GRB direction in Galactic and equatorial coordinates, two different estimates of GRB time duration, i.e., the classical  $T_{90}$  (time during which the burst integrated counts increase from 5% to 95% of the total counts, Kouveliotou et al. 1993) and the time duration  $T_{\text{det}}$  (see below), the integrated time  $T_a$  during which the burst count rate is detected above a  $2\sigma$  level, the 40–700 keV fluence, peak flux, the spectral hardness, the GRBM units used for the parameters determination, the binning factor with respect to the default count accumulation time (1 s for long GRBs, 7.8125 ms in the case of short GRBs). For different reasons not all the parameters were determined for the entire GRBs sample (see details in Table 3). Details on the data reported and on methods adopted for the derivation of the parameters reported in the catalog are given below.

### 7.1. GRB coordinates

For each event, we report the most accurate equatorial (at the epoch 2000.0) and Galactic coordinates available. When a GRB was detected by more than one experiment, the more plausibly precise localization is given. When the GRB was detected by one of the WFCs on board *BeppoSAX* other possible detections are ignored. For the GRBs detected by only GRBM and for which the localization procedure has given a unique position, the GRBM direction estimate is reported. In the column *CAT* of the catalog we report the instrument or mission that provided the best GRB coordinates.

## 7.2. Detection units used for the parameter derivation

For each GRB, we give in the column *Unit* the GRBM units used to derive the parameters reported in the catalog. The first number of the column identifies, for each GRB, the GRBM unit used for the determination of  $T_{90}$ ,  $T_{\text{det}}$  and  $T_a$ . This unit provided the light curve with the best signal-to-noise ratio. The second number gives the GRBM unit used for the determination of the GRB fluence, peak flux and spectral hardness  $\Gamma$ . When it was possible to improve the statistical quality of the results, the signal from another unit was added in (third number). These two units have the lowest angular distance from the GRB.

## 7.3. GRB Duration

We report two different estimates of the GRB time duration in the 40–700 keV energy band. The first one is the usual  $T_{90}$  as defined by the BATSE team (Kouveliotou et al. 1993). The technique adopted is described by Koshut et al. (1996) and it applies to the background subtracted light curves. This method is applied to both 1 s and 7.8125 ms light curves. For the  $T_{90}$  estimate, we have used the most illuminated unit.

The second estimate of the GRB duration is  $T_{\text{det}}$ , that gives the time elapsed from the earliest GRB onset above a  $2\sigma$  threshold to its final disappearance below  $2\sigma$ . In the case of long GRBs ( $\geq 2$  s), the error associated to  $T_{\text{det}}$  was given by  $R/\sqrt{2}$ , where  $R$  is the rebinning time listed in the column *R* of Table 2, while in the case of short GRBs, this error was assumed to be equal to  $R$ . In addition to  $T_{\text{det}}$ , for each GRB we report in the catalog the integrated time  $T_a$  in which the burst was visible above a  $2\sigma$  level and the number  $N_a$  of intervals in which the  $2\sigma$  level was exceeded in the time profile. The error associated to  $T_a$  was determined assuming an uncertainty of  $R/\sqrt{2}$  for each of the  $N_a$  intervals. From  $T_a$  an estimate of the integrated quiescent time  $T_q$  of each GRB can be derived.

For short GRBs with available high time resolution data (112 events), the  $T_{\text{det}}$  estimate was obtained from the 7.8125 ms light curves. For the  $T_a$  determination, the  $2\sigma$  level was derived using the Poissonian distribution, i.e. determining the count threshold  $n_{th}$  such that, if the count rate  $n$  is higher than  $n_{th}$ , the probability that this count excess is due to a Poissonian fluctuation is lower than 5%.

#### 7.4. Fluence and spectral hardness

Using the GRBM response function discussed above, and the XSPEC software package, for each GRB, its 40–700 keV fluence has been derived from the 2 channel background-subtracted spectra (40–700 keV and  $> 100$  keV) integrated over  $T_{\text{det}}$  with the assumption of a power-law (PL) spectrum. We refer to these spectra as “2-channel spectra”. The power-law spectral index  $\Gamma$  derived is reported in the column  $\Gamma$  of the catalog. The PL model was a forced choice for those GRBs for which the 240-channel spectra (integrated over 128 s) did not provide useful results. Given that the PL choice could introduce a systematic error in the fluence estimate, we corrected the fluences derived from the 2-channel spectra in the following way. Using the strong GRBs (163) for which both the 2-channel and 240-channel spectra could be used, we compared the fluence estimates derived from the 2-channel spectra with those derived from the dead-time corrected 240-channel spectra, in which the best input spectral model was adopted. Thus we derived an average correction factor  $CF$ , that was used to correct the 2-channel fluences. This factor was found to approximately show a Gaussian distribution with a  $\sigma \sim 0.01$  and no significant dependence on GRB fluence.

#### 7.5. Peak Flux

For the 40–700 keV peak flux estimate, we adopted the same procedure followed for the fluence estimate. Using the GRBM response function and assuming a PL model, for long GRBs, we deconvolved the 40–700 keV the peak counts over the minimum time interval around the peak that gave a significant peak flux estimate. For long GRBs, in general, we used the 1 s background-subtracted light curves in the two (40–700 keV and  $> 100$  keV) energy channels. However, for those GRBs for which the 1 s light curves provided a peak count rate with a signal-to-noise ratio lower than 3, a rebinning of the data was performed. The rebinning factor  $R$  is given in the last column of the catalog (a value of 1 corresponds to 1 s light curves).

For short GRBs, we first derived the 40–700 keV peak flux  $F_p^{1s}$  from the 1 s light curves as above. Given that a 1 s integration time is too long, we corrected  $F_p^{1s}$  for the ratio  $R_C$  between the 125 ms 40–700 keV peak count rate  $C_p^{125ms}$  normalized to a 1 s time and the corresponding 1 s peak count rate  $C_p^{1s}$  adopted for the deconvolution of the two-channel spectra. The reported 40–700 keV peak flux is given by  $F_p = F_p^{1s} \times R_C$ .

## 8. Results of statistical analysis of the catalog

We performed a statistical analysis of the data reported in the GRBM Catalog, for checking their mutual consistency, for comparing our results with those obtained with BATSE, and for getting new results.

### 8.1. Consistency tests

We tested the dependence of the  $T_{\text{det}}$  estimate on  $T_{90}$ . The result is shown in Fig. 4. We find that, within statistical uncertainties,  $T_{\text{det}}$  is fully correlated with  $T_{90}$ , as expected. In principle, we would expect to get  $T_{\text{det}}$  equal or longer than  $T_{90}$ . However, for some weak GRBs, this expectation is not satisfied, mainly due to the larger uncertainty in the determination of the  $T_{\text{det}}$  estimate with respect to that of  $T_{90}$ .

The distributions of the GRB peak flux and fluence are shown in Fig. 5. As can be seen, both are clearly skewed, as expected as a consequence of the GRBM sensitivity threshold. We derive from these Figures the limit sensitivity of the GRBM: it is  $\sim 4 \times 10^{-8} \text{ erg cm}^{-2} \text{ s}^{-1}$  in terms of peak flux , while it is about  $\sim 2 \times 10^{-7} \text{ erg cm}^{-2}$  in terms of fluence. Also the hardness distribution for short and long GRBs has been derived and shown in Fig. 6. As can be seen the distribution derived for long GRBs is almost symmetrical with a mean value  $\Gamma_{\text{long}} \simeq 2$  and a saturation around  $\Gamma \simeq 3$ , likely due to the limited sensitivity of the instrument at high photon energies. Instead that derived for short GRBs is asymmetrical with a positive skewness and a mean value of  $\Gamma_{\text{short}} \simeq 1.5$ . At a significance level of  $3.2 \times 10^{-5}$ , we find that of the  $\Gamma$  mean value the long GRBs is higher than that of short GRBs.

### 8.2. Comparison with the BATSE results

The first test performed is the spatial distribution of the detected GRBs in the sky. The result is shown in Fig. 7. We confirm the isotropical distribution of the GRBs as found by BATSE (Fishman et al. 1994; Paciesas et al. 1999). In Table 4 we report the corresponding statistical results for detecting a Galactic association, i.e., our measures of the dipole and quadrupole moments (Briggs 1993) in Galactic and equatorial coordinates.

We also derived the  $\log N - \log S$  and  $\log N - \log P$  distributions, where  $N$  is the number of GRBs with the 40–700 keV fluence  $S$  (or 40–700 keV peak flux  $P$ ) higher than given values. The results are shown in Fig. 8. To compare our results with those derived with BATSE in the 50–300 keV energy range (e.g. Paciesas et al. 1999), we first estimated the

GRB fluence and peak flux in the 50–300 keV using the derived power-law spectral index  $\Gamma$ . The derived distributions compared with those obtained with BATSE are shown in Fig. 9. Using a Kolmogorov-Smirnov (KS) test, we find that at a significance level of 1% the GRBM and BATSE log  $N$ –log  $S$  distributions are consistent for fluences  $> 1 \times 10^{-6}$  erg cm $^{-2}$  while at a significance level of 5% the log  $N$ –log  $P$  distributions are consistent with each other for peak fluxes  $> 1 \times 10^{-7}$  erg cm $^{-2}$  s $^{-1}$ .

The distributions of the GRBM GRBs with  $T_{90}$  and  $T_{\text{det}}$  have also been investigated. Both distributions are similar. The results for  $T_{90}$  are shown in Fig. 10. As can be seen, the bimodal behavior found with BATSE (see, e.g., Kouveliotou et al. 1993) is confirmed, even if the distribution of  $T_{90}$  for short GRBs appears less pronounced and displaced toward higher durations with respect to BATSE. This discrepancy is due to the lower efficiency of our trigger system to short GRBs, which, for almost the entire mission duration, used 1 s as short integration time (see Table 1). This bias does not allow to test the presence of a third class of GRBs as claimed by Horváth et al. (2008).

We have also investigated the dependence of the GRB hardness  $\Gamma$  as a function of the time duration  $T_{90}$ . The result is shown in Fig. 11. While it is apparent that there is no correlation of  $\Gamma$  with the GRB time duration within either the long or the short GRBs, using the nonparametric Spearman and Kendall correlation tests, we find a slight correlation (significance level of 2%) between  $\Gamma$  and GRB duration when both short and long GRBs are taken into account. This result confirms the result found using the  $\Gamma$  distribution of long and short GRBs (see section 8.1).

### 8.3. Other tests

In addition to the previous tests, other tests have been derived from our catalog, thanks to the determination of  $T_{\text{det}}$  and of the activity time  $T_a$ .

In Fig. 12 we show the distribution of  $T_a$  compared with that of  $T_{\text{det}}$ . As can be seen, the maximum activity time detected is about 200 s, whereas we find GRBs with  $T_{\text{det}}$  up to 600 s.

In Fig. 13 we show the cumulative distribution of the integrated active time  $T_a$ . As can be seen from this figure and as found from a Shapiro-Wilk test (Shapiro & Wilk 1965), for short GRBs, this distribution is consistent with a log-normal distribution ( $p$ -value of 0.58) in the case of short GRBs, while it is inconsistent with the latter ( $p$ -value of  $4.6 \times 10^{-8}$ ) in the case of long GRBs. In Fig. 14 we show the cumulative distribution of the integrated quiescent time  $T_q$  obtained by subtracting  $T_a$  from  $T_{\text{det}}$ . As can be seen from this figure and

from the Shapiro–Wilk test, for either short and long GRBs this distribution is inconsistent with a log-normal, with a lower probability chance for long GRBs ( $p$ –value of  $1.9 \times 10^{-4}$  in the case of short GRBs against a  $p$ –value of  $7.5 \times 10^{-8}$  in the case of long GRBs).

## 9. Discussion

The first complete catalog of the GRBs detected with the *BeppoSAX* GRBM includes 1082 GRBs, for most of which we have reported complete information (position, duration, peak flux, fluence and spectral hardness).

Concerning the GRB positions, we have reported the most accurate coordinates available for each GRBs included in the catalog. In the next future, for some of them, more accurate (or the first determination of) positions will be available from the Inter–Planetary Network (K. Hurley et al., in preparation), allowing a more accurate determination (or the first determination) of the fluence and peak flux values.

Some relevant results obtained with the BATSE catalogs (e.g., isotropical distribution of GRBs in the sky, deviation of the  $\log N$ – $\log S$  and  $\log N$ – $\log P$  cumulative distributions from that expected in the case of an homogeneous distribution of GRBs in an Euclidean space, two–peak distribution of the GRBs with time duration, higher hardness of the short GRBs) are confirmed.

For the first time, our catalog includes, in addition to the classical  $T_{90}$  GRB duration, also the total duration  $T_{\text{det}}$  and the integrated time  $T_a$  during which the GRB intensity exceeds the  $2\sigma$  level. We find that the GRB active time has a cutoff at about 200 s, in spite that we find GRBs with  $T_{\text{det}}$  up to 600 s. This result can have a relation with the physics of the unknown engine that gives rise to the GRBs. It seems that this engine has a maximum active time of 200 s. The integrated active is found consistent with a log-normal distribution for either short and long GRBs.

The origin of quiescent times is still unknown. The quiescent time properties have been investigated by various authors (Nakar & Piran 2002; Drago & Pagliara 2007). We limit our investigation to the active time  $T_a$  and quiescent time  $T_q$ , both integrated over the entire GRB duration. In the case of  $T_a$ , we find that its distribution is consistent with a log-normal distribution for short GRBs, while it is inconsistent with the latter in the case of long GRBs. In the case of the integrated  $T_q$ , we find that the cumulative distribution is inconsistent with a log-normal distribution in the case of short and long GRBs. The consequences of these results would require further discussion, which is beyond the scope of this paper. We limit us to state that models of GRB engines and of their behavior with time should take into

account these statistical results.

Many people contributed to the success of the GRBM instrument. We wish to thank all of them. The *BeppoSAX* mission was a joint program of the Italian space agency ASI and of the Netherlands Agency for Aerospace Programs. This research was supported by the Ministry of Education, University and Research of Italy (PRIN 2005-025417 devoted to GRBs).

## REFERENCES

- Amati, L., Cinti, M. N., Feroci, M., Costa, E., Frontera, F., dal Fiume, D., Collina, P., Nicastro, L., Orlandini, M., Palazzi, E., Rapisarda, M., & Zavattini, G. 1997, in Proc. SPIE Vol. 3114, p. 176-185, EUV, X-Ray, and Gamma-Ray Instrumentation for Astronomy VIII, Oswald H. Siegmund; Mark A. Gummin; Eds., ed. O. H. Siegmund & M. A. Gummin, 176–185
- Boella, G., Chiappetti, L., Conti, G., Cusumano, G., del Sordo, S., La Rosa, G., Maccarone, M. C., Mineo, T., Molendi, S., Re, S., Sacco, B., & Tripiciano, M. 1997, A&AS, 122, 327
- Briggs, M. S. 1993, ApJ, 407, 126
- Brown, F. e. a. 2002, Trans. Am. Nucl. Soc., 87, 273
- Calura, F., Rapisarda, M., Frontera, F., Montanari, E., Guidorzi, C., Amati, L., Feroci, M., Costa, E., & Collina, P. 2000, in AIP Conf. Proc. 526: Gamma-ray Bursts, 5th Huntsville Symposium, ed. R. M. Kippen, R. S. Mallozzi, & G. J. Fishman, 721
- Costa, E., Frontera, F., dal Fiume, D., Amati, L., Cinti, M. N., Collina, P., Feroci, M., Nicastro, L., Orlandini, M., Palazzi, E., Rapisarda, M., & Zavattini, G. 1998, Advances in Space Research, 22, 1129
- Costa, E., Frontera, F., Heise, J., Feroci, M., in 't Zand, J., Fiore, F., Cinti, M. N., dal Fiume, D., Nicastro, L., Orlandini, M., Palazzi, E., Rapisarda, M., Zavattini, G., Jager, R., Parmar, A., Owens, A., Molendi, S., Cusumano, G., Maccarone, M. C., Giarrusso, S., Coletta, A., Antonelli, L. A., Giommi, P., Muller, J. M., Piro, L., & Butler, R. C. 1997, Nature, 387, 783
- Drago, A., & Pagliara, G. 2007, ApJ, 665, 1227

- Feroci, M., Frontera, F., Costa, E., dal Fiume, D., Amati, L., Bruca, L., Cinti, M. N., Coletta, A., Collina, P., Guidorzi, C., Nicastro, L., Orlandini, M., Palazzi, E., Rapisarda, M., Zavattini, G., & Butler, R. C. 1997, in Proc. SPIE Vol. 3114, p. 186-197, EUV, X-Ray, and Gamma-Ray Instrumentation for Astronomy VIII, Oswald H. Siegmund; Mark A. Gummin; Eds., ed. O. H. Siegmund & M. A. Gummin, 186–197
- Fishman, G. J., Meegan, C. A., Wilson, R. B., Brock, M. N., Horack, J. M., Kouveliotou, C., Howard, S., Paciesas, W. S., Briggs, M. S., Pendleton, G. N., Koshut, T. M., Mallozzi, R. S., Stollberg, M., & Lestrade, J. P. 1994, ApJS, 92, 229
- Frail, D. A., Kulkarni, S. R., Nicastro, L., Feroci, M., & Taylor, G. B. 1997, Nature, 389, 261
- Frontera, F. 2004, in Astronomical Society of the Pacific Conference Series, ed. M. Feroci, F. Frontera, N. Masetti, & L. Piro, 3–11
- Frontera, F., Costa, E., dal Fiume, D., Feroci, M., Nicastro, L., Orlandini, M., Palazzi, E., & Zavattini, G. 1997, A&AS, 122, 357
- Guidorzi, C. 2002, PhD thesis, Physics Department, University of Ferrara
- Guidorzi, C., Amati, L., Feroci, M., Costa, E., Frontera, F., dal Fiume, D., & Orlandini, M. 1998, in The Active X-ray Sky: Results from BeppoSAX and RXTE, ed. L. Scarsi, H. Bradt, P. Giommi, & F. Fiore, 664
- Guidorzi, C., Frontera, F., Montanari, E., F., C., , Amati, L., Costa, E., & M., F. 2001, in Gamma Ray Bursts in the Afterglow Era, ed. E. Costa, F. Frontera, & J. Hjorth, 43
- Horváth, I., Balázs, L. G., Bagoly, Z., & Veres, P. 2008, A&A, 489, L1
- Jager, R., Mels, W. A., Brinkman, A. C., Galama, M. Y., Goulooze, H., Heise, J., Lowes, P., Muller, J. M., Naber, A., Rook, A., Schuurhof, R., Schuurmans, J. J., & Wiersma, G. 1997, A&AS, 125, 557
- Kaneko, Y., Preece, R. D., Briggs, M. S., Paciesas, W. S., Meegan, C. A., & Band, D. L. 2006, ApJS, 166, 298
- Kommers, J. M., Lewin, W. H. G., Kouveliotou, C., van Paradijs, J., Pendleton, G. N., Meegan, C. A., & Fishman, G. J. 2001, ApJS, 134, 385
- Koshut, T. M., Paciesas, W. S., Kouveliotou, C., van Paradijs, J., Pendleton, G. N., Fishman, G. J., & Meegan, C. A. 1996, ApJ, 463, 570

- Kouveliotou, C., Meegan, C. A., Fishman, G. J., Bhat, N. P., Briggs, M. S., Koshut, T. M., Paciesas, W. S., & Pendleton, G. N. 1993, *ApJ*, 413, L101
- Meegan, C. A., Pendleton, G. N., Briggs, M. S., Kouveliotou, C., Koshut, T. M., Lestrade, J. P., Paciesas, W. S., McCollough, M. L., Brainerd, J. J., Horack, J. M., Hakkila, J., Henze, W., Preece, R. D., Mallozzi, R. S., & Fishman, G. J. 1996, *ApJS*, 106, 65
- Metzger, M. R., Djorgovski, S. G., Kulkarni, S. R., Steidel, C. C., Adelberger, K. L., Frail, D. A., Costa, E., & Frontera, F. 1997, *Nature*, 387, 878
- Nakar, E., & Piran, T. 2002, *MNRAS*, 331, 40
- Paciesas, W. S., Meegan, C. A., Pendleton, G. N., Briggs, M. S., Kouveliotou, C., Koshut, T. M., Lestrade, J. P., McCollough, M. L., Brainerd, J. J., Hakkila, J., Henze, W., Preece, R. D., Connaughton, V., Kippen, R. M., Mallozzi, R. S., Fishman, G. J., Richardson, G. A., & Sahi, M. 1999, *ApJS*, 122, 465
- Rapisarda, M., Amati, L., Cinti, M. N., Feroci, M., Costa, E., Collina, P., Zavattini, G., Frontera, F., Nicastro, L., Orlandini, M., Palazzi, E., & dal Fiume, D. 1997, in *Proc. SPIE Vol. 3114*, p. 198-205, EUV, X-Ray, and Gamma-Ray Instrumentation for Astronomy VIII, Oswald H. Siegmund; Mark A. Gummin; Eds., ed. O. H. Siegmund & M. A. Gummin, 198–205
- Shapiro, S. S., & Wilk, M. B. 1965, *Biometrika*, 52, 591
- Stern, B. E., Tikhomirova, Y., Kompaneets, D., Svensson, R., & Poutanen, J. 2001, *ApJ*, 563, 80
- Toor, A., & Seward, F. D. 1974, *AJ*, 79, 995
- van Paradijs, J., Groot, P. J., Galama, T., Kouveliotou, C., Strom, R. G., Telting, J., Rutten, R. G. M., Fishman, G. J., Meegan, C. A., Pettini, M., Tanvir, N., Bloom, J., Pedersen, H., Nordgaard-Nielsen, H. U., Linden-Vornle, M., Melnick, J., van der Steene, G., Bremer, M., Naber, R., Heise, J., in 't Zand, J., Costa, E., Feroci, M., Piro, L., Frontera, F., Zavattini, G., Nicastro, L., Palazzi, E., Bennet, K., Hanlon, L., & Parmar, A. 1997, *Nature*, 386, 686

Table 1. GRBM trigger parameter and energy threshold settings.

Epoch	Trigger parameters			Energy thresholds		
	LIT (s)	SIT (s)	$n_\sigma$	LLT (keV)	ULT (keV)	ACT (keV)
Mission start time	128	4	8	32.8	700	100
30 October 1996	128	1	4	42.5	700	100
28 November 1996	32	1	4	42.5	700	100
January 2002	32	0.125	4	42.5	700	100







































Table 3. GRBs statistics

GRB type	Number
GRBs with all parameters determined	764
GRBs with only information about duration	266
GRBs with gaps in the data	42
GRBs without $F_{\text{peak}}$ because of low statistics	10
Total GRBs	1082

Table 4. Dipole and quadrupole statistics for the GRBs detected by the *BeppoSAX* GRBM with determined direction

Tested Moment	Moment Type	Coordinate System	Measured Value	Expected value <sup>a</sup>
$\langle \cos \theta \rangle$	Dipole	Galactic	$-0.015 \pm 0.020$	$0.000 \pm 0.009$
$\langle \sin \delta \rangle$	Dipole	Equatorial	$0.026 \pm 0.020$	$0.000 \pm 0.009$
$\langle \sin^2 b - 1/3 \rangle$	Quadrupole	Galactic	$-0.003 \pm 0.010$	$-0.007 \pm 0.005$
$\langle \sin^2 \delta - 1/3 \rangle$	Quadrupole	Equatorial	$0.038 \pm 0.010$	$0.039 \pm 0.005$

<sup>a</sup>for an isotropic distribution and corrected for the sky exposure map

Note. —  $\theta$  is the angle between the direction to the burst and the Galactic center,  $b$  is the Galactic latitude,  $\delta$  is GRB declination.

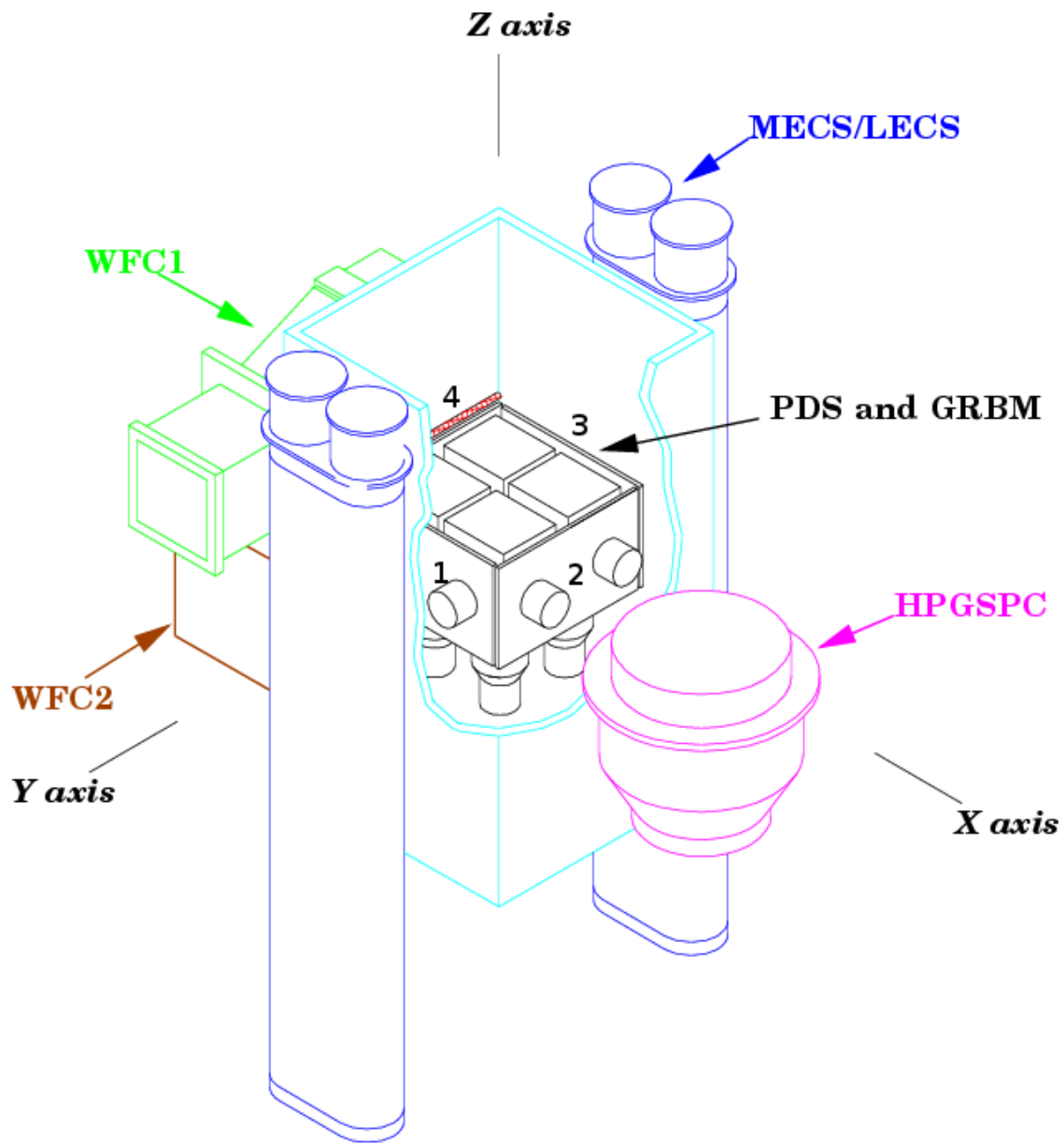


Fig. 1.— The *BeppoSAX* payload, in which the location of the GRBM units is shown.

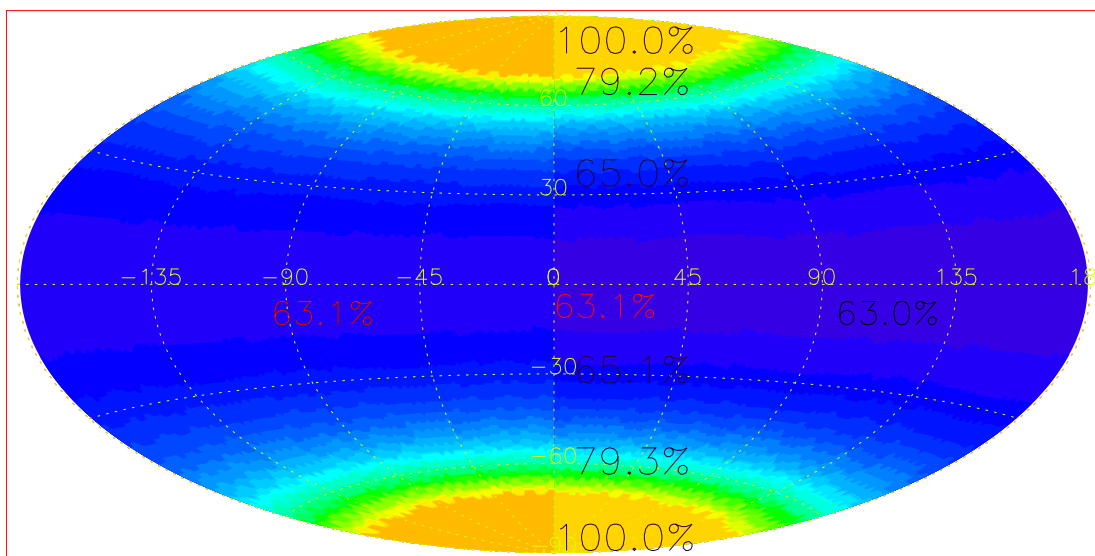


Fig. 2.— Fraction of time in which a given sky direction, in celestial coordinates, was exposed to the GRBM.

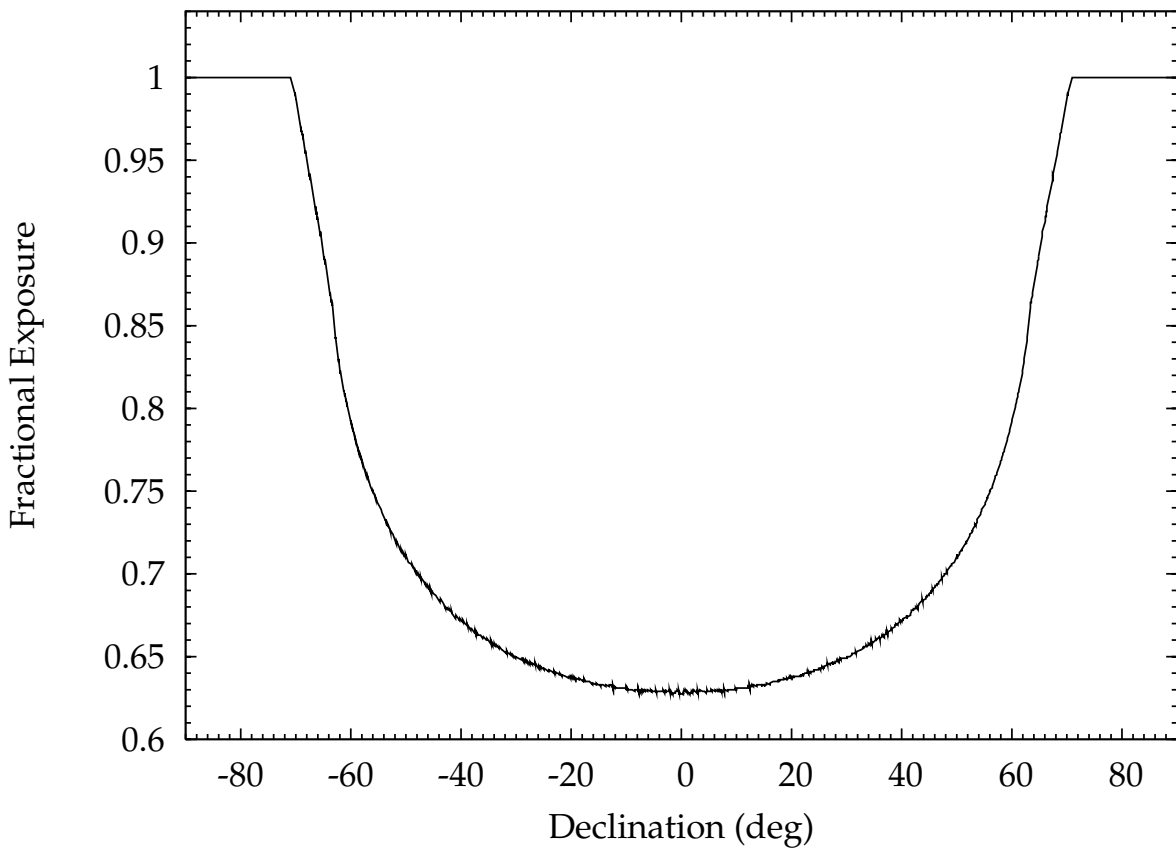


Fig. 3.— Fraction of the GRBM exposure time versus celestial declination after averaging the sky exposure over the right ascension.

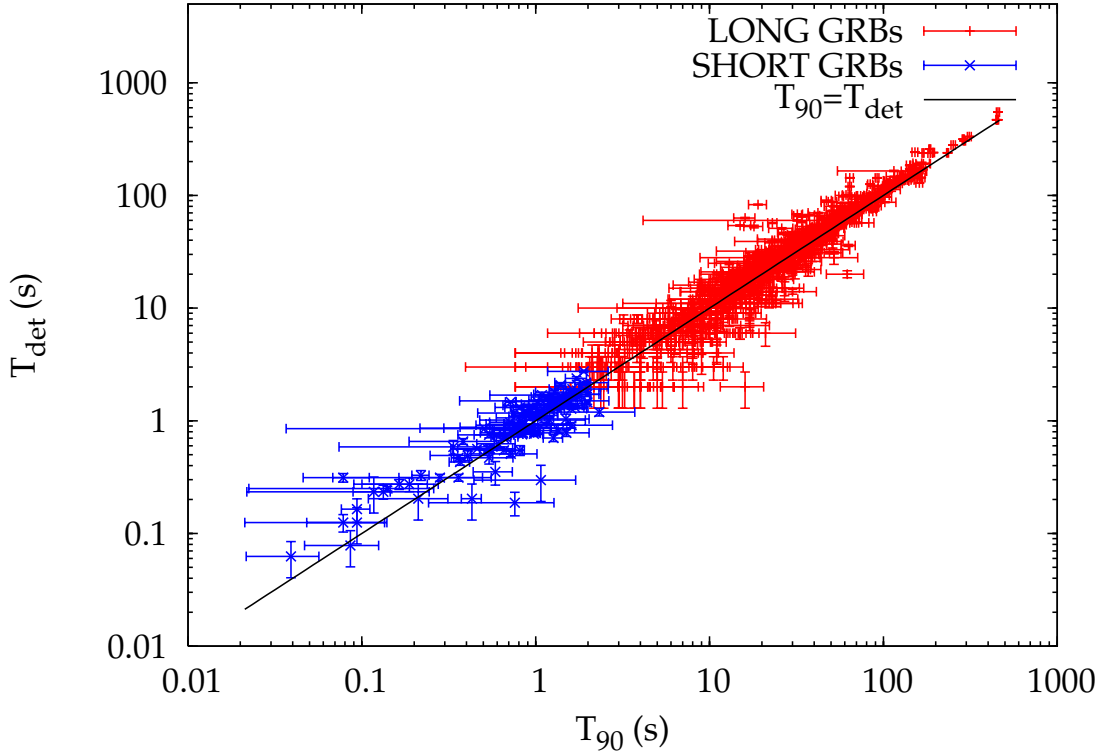


Fig. 4.— Correlation between  $T_{90}$  and  $T_{\text{det}}$  GRB time durations. Short GRBs in blue color. The central continuous line gives the curve  $T_{90} = T_{\text{det}}$ .

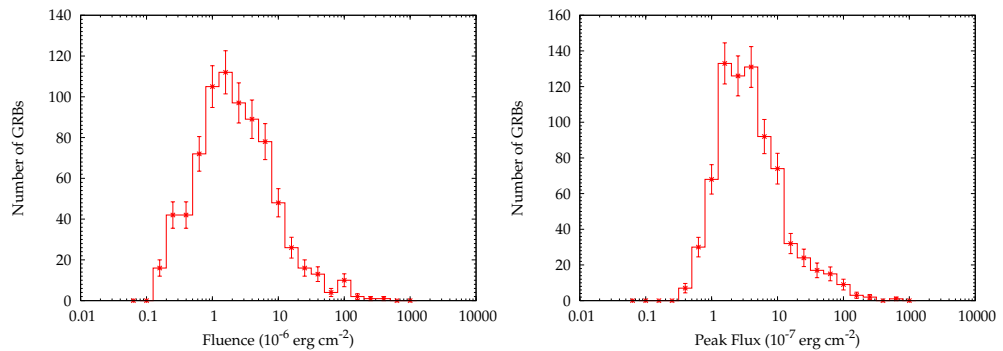


Fig. 5.— Distribution of fluence (*left*) and peak flux (*right*) of the GRBs detected with the *BeppeSAX* GRBM.

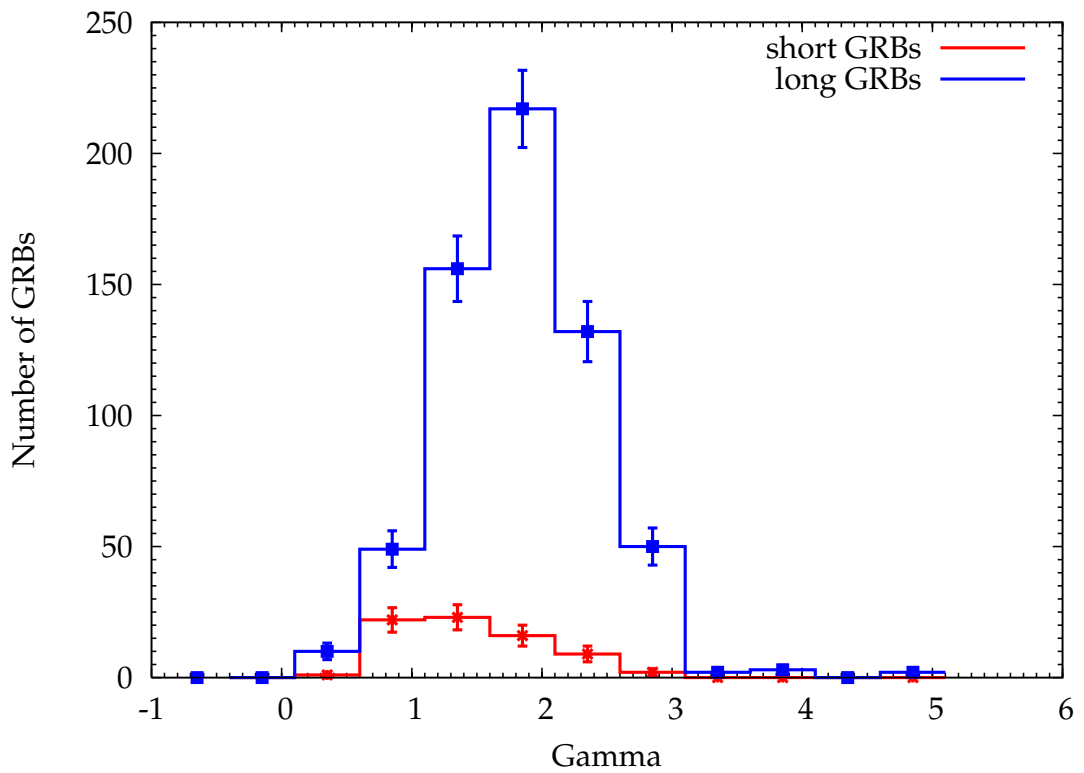


Fig. 6.— Distribution of the GRB spectral hardness for short and long GRBs. The GRB hardness is defined as the index  $\Gamma$  of the best power-law fit to the 2-channel spectra.

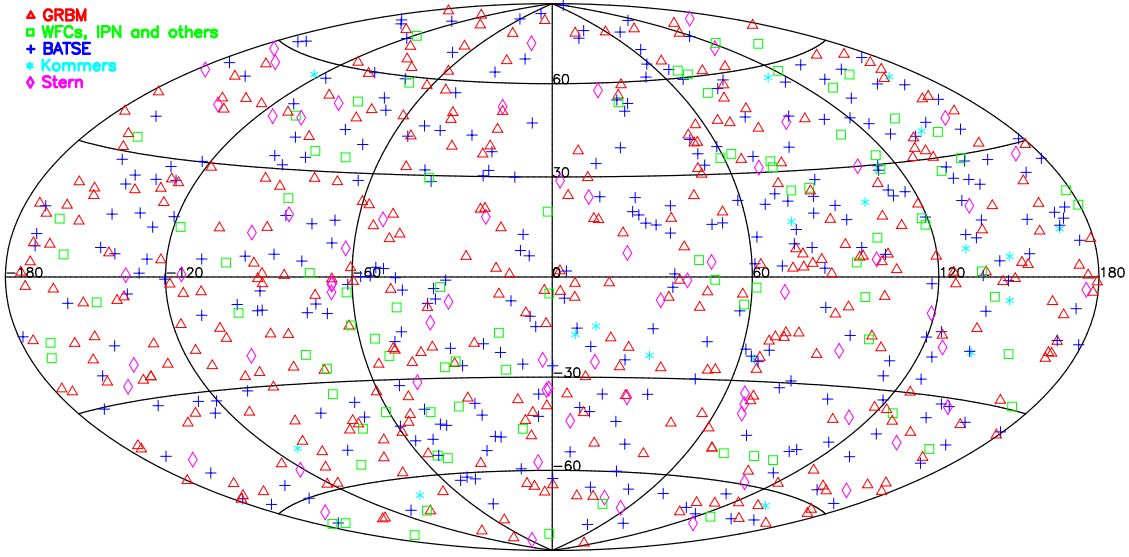


Fig. 7.— Sky distribution (in Galactic coordinates) of GRBs detected with the *BeppoSAX* GRBM. In different colors and symbols the GRB also found in other catalogs found with other instrumentation. Also the GRBs identified with the *BeppoSAX* WFCs are shown.

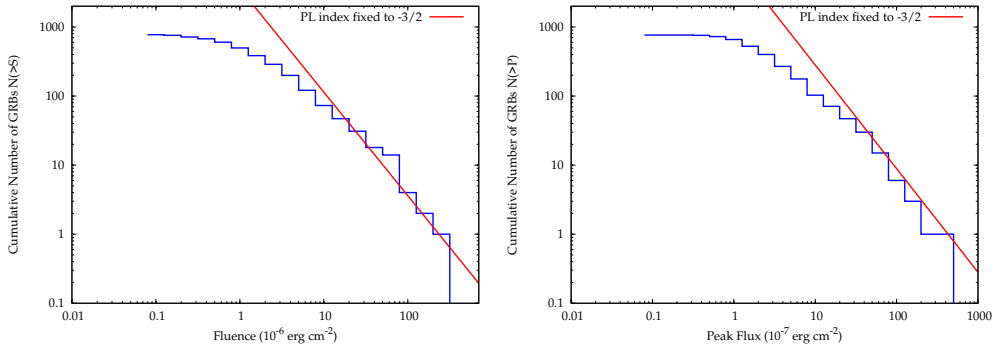


Fig. 8.— Cumulative distribution of the 40–700 keV fluence (left panel) and peak flux (right panel) of the GRBs detected with the *BeppoSAX* GRBM. The continuous line gives the distribution (a power-law of index  $-3/2$ ) that is expected in the case the observed GRBs are homogeneously distributed in an Euclidian space throughout the sampled volume.

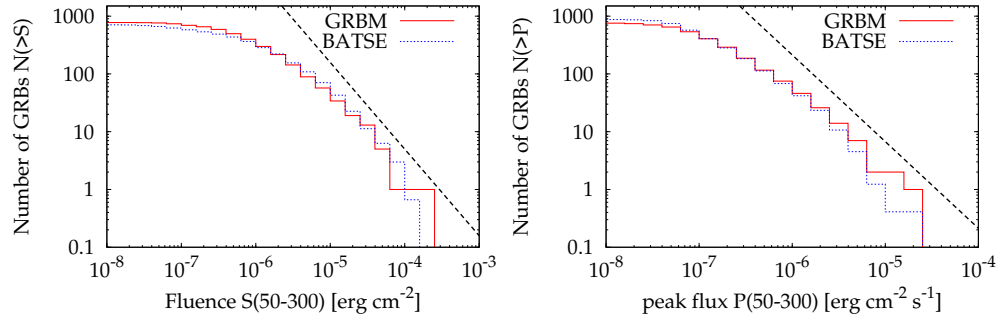


Fig. 9.— Comparison of the *BeppoSAX* GRBM and BATSE 50–300 keV fluence (left panel) and peak flux (right panel) cumulative distributions. The continuous line gives the distribution (a power-law of index  $-3/2$ ) that is expected in the case the observed GRBs are homogeneously distributed in an Euclidian space throughout the sampled volume.

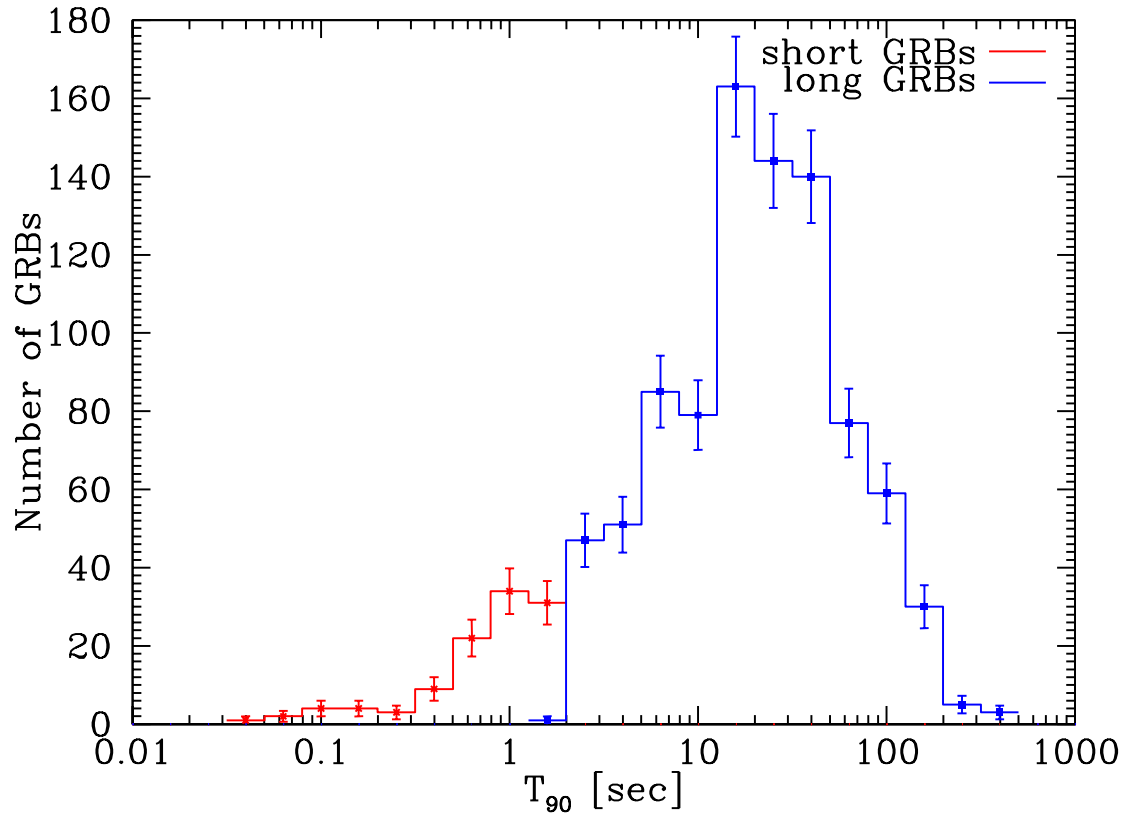


Fig. 10.— Distribution of the GRBM GRBs according to their  $T_{90}$  duration. Only short GRB triggered by the on board logic were included. *In red color:* short GRBs; *in blue color:* long GRBs.

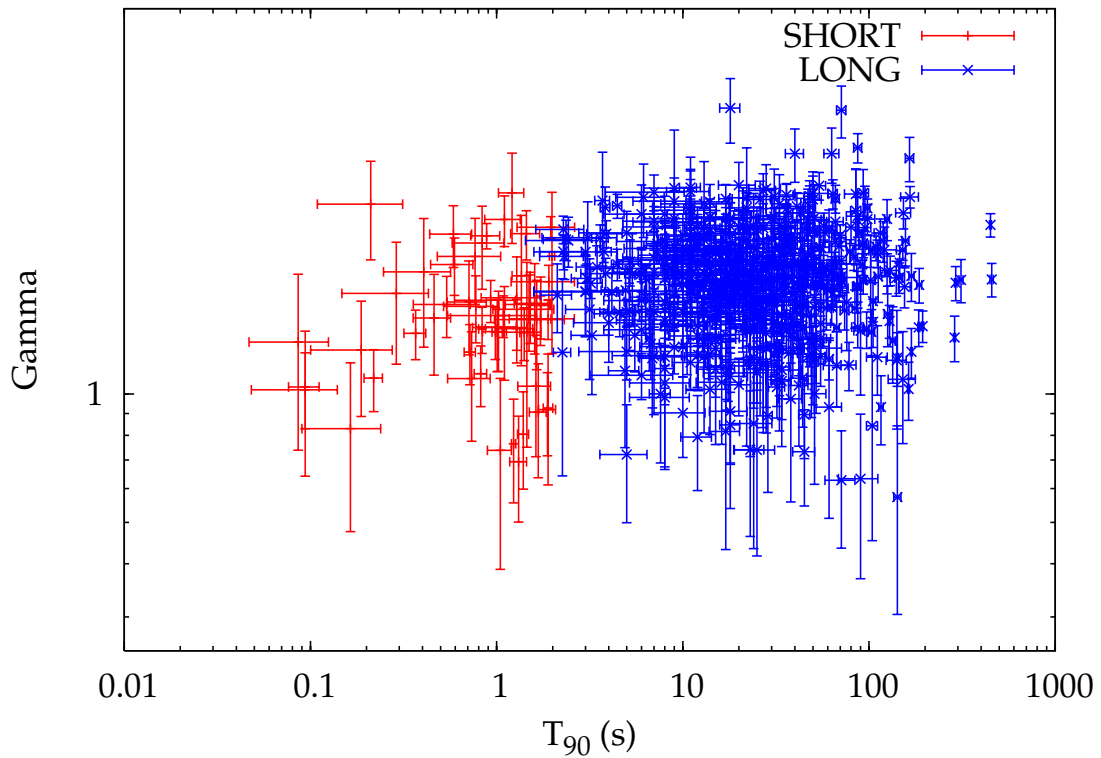


Fig. 11.— Dependence of the GRB hardness on  $T_{90}$  duration. As hardness parameter we use the power-law photon index  $\Gamma$  listed in the Catalog. *In red color:* short GRBs; *in blue color:* long GRBs.

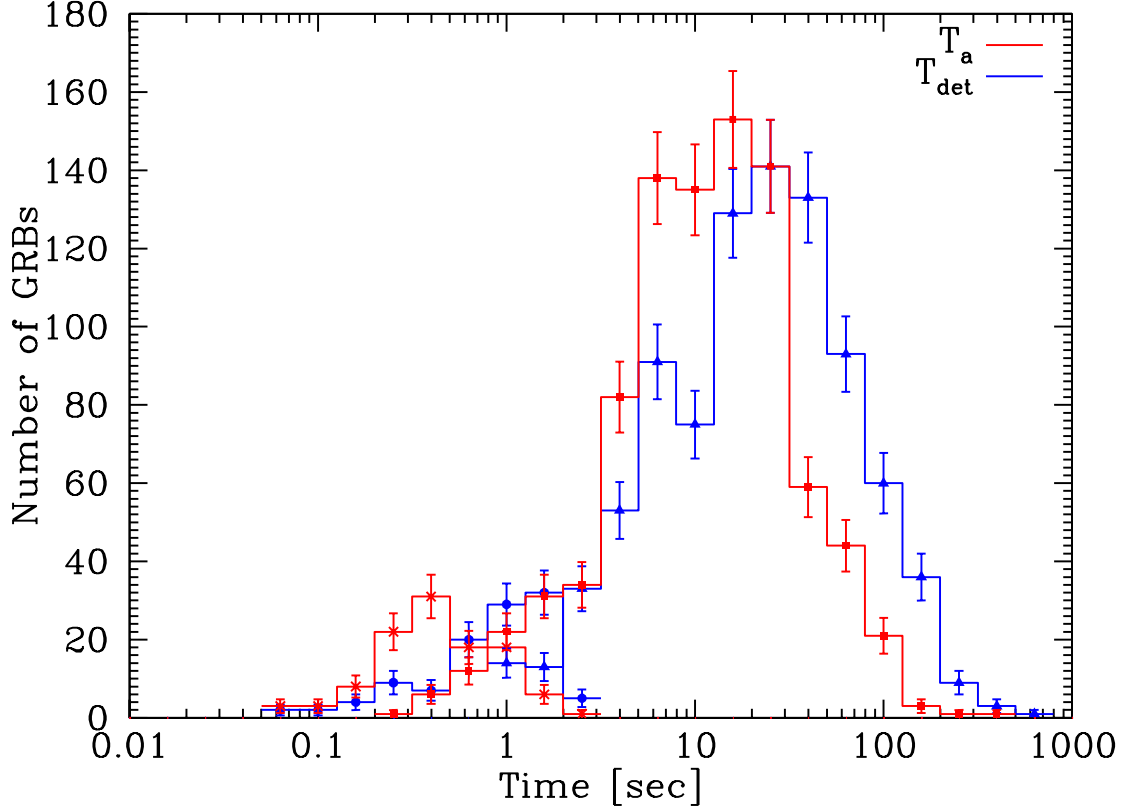


Fig. 12.— Distribution of the integrated active emission time  $T_a$  (red) compared with the total duration  $T_{\text{det}}$  (blue). Symbols for  $T_{\text{det}}$ : filled triangles for long GRBs, filled circles for short GRBs. Symbols for  $T_a$ : filled squares for long GRBs, stars for short GRBs.

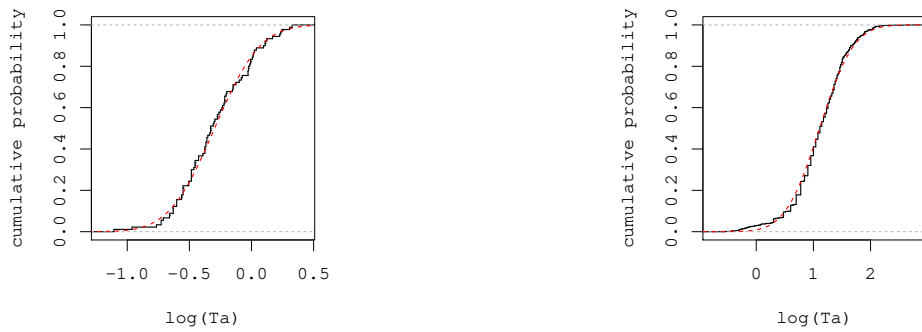


Fig. 13.— Cumulative distribution of the active time  $T_a$  compared with that expected from a log-normal distribution (dashed line). *Left panel:* short GRBs; *right panel:* long GRBs.

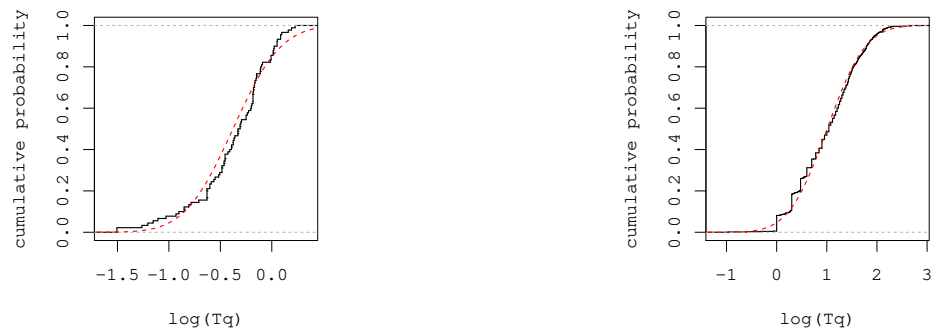


Fig. 14.— Cumulative distribution of the quiescent time  $T_q$  compared with that expected from a log-normal distribution (dashed line). *Left panel:* short GRBs; *right panel:* long GRBs.